J. Fluid Mech. (2010), *vol.* 656, *pp.* 481–506.
doi:10.1017/S0022112010001254

Dynamics and stability of an annular electrolyte film

D. T. CONROY[1], R. V. CRASTER[2]†, O. K. MATAR[1] AND D. T. PAPAGEORGIOU[1,3]

[1]Department of Chemical Engineering, Imperial College London, South Kensington Campus, London SW7 2AZ, UK

[2]Department of Mathematical and Statistical Sciences, University of Alberta, Edmonton, Alberta T6G 2G1, Canada

[3]Department of Mathematics, Imperial College London, South Kensington Campus, London SW7 2AZ, UK

(Received 30 October 2009; revised 8 March 2010; accepted 8 March 2010; first published online 26 May 2010)

We investigate the evolution of an electrolyte film surrounding a second electrolyte core fluid inside a uniform cylindrical tube and in a core-annular arrangement, when electrostatic and electrokinetic effects are present. The limiting case when the core fluid electrolyte is a perfect conductor is examined. We analyse asymptotically the thin annulus limit to derive a nonlinear evolution equation for the interfacial position, which accounts for electrostatic and electrokinetic effects and is valid for small Debye lengths that scale with the film thickness, that is, charge separation takes place over a distance that scales with the annular layer thickness. The equation is derived and studied in the Debye-Hückel limit (valid for small potentials) as well as the fully nonlinear Poisson–Boltzmann equation. These equations are characterized by an electric capillary number, a dimensionless scaled inverse Debye length and a ratio of interface to wall electrostatic potentials. We explore the effect of electrokinetics on the interfacial dynamics using a linear stability analysis and perform extensive numerical simulations of the initial value problem under periodic boundary conditions. An allied nonlinear analysis is carried out to investigate fully singular finite-time rupture events that can take place. Depending upon the parameter regime, the electrokinetics either stabilize or destabilize the film and, in the latter case, cause the film to rupture in finite time. In this case, the final film shape can have a ring- or line-like rupture; the rupture dynamics are found to be self-similar. In contrast, in the absence of electrostatic effects, the film does not rupture in finite time but instead evolves to very long-lived quasi-static structures that are interrupted by an abrupt re-distribution of these very slowly evolving drops and lobes. The present study shows that electrokinetic effects can be tuned to rupture the film in finite time and the time to rupture can be controlled by varying the system parameters. Some intriguing and novel behaviour is also discovered in the limit of large scaled inverse Debye lengths, namely stable and smooth non-uniform steady state film shapes emerge as a result of a balance between destabilizing capillary forces and stabilizing electrokinetic forces.

† Email address for correspondence: craster@ualberta.ca

1. Introduction

Annular thin films, either exterior or interior to a rigid cylindrical wall, consist of a liquid layer of small radial extent adjacent to the wall, separating it from another liquid or a gas. Understanding this core-annular arrangement, or its exterior analogue, is important to a number of applications. These include the flows of the liquid lining of pulmonary airways (Grotberg & Jensen 2004), liquid–liquid displacements in porous media for either oil recovery or carbon sequestration (Olbricht 1996; Maitland 2000), coating flows either on the inside of a cylinder or outside of a fibre (Kalliadasis & Chang 1994; Chang & Demekhin 1999; Quéré 1999; Craster & Matar 2006; Ruyer-Quil *et al.* 2008), which are of interest to heat exchangers and condensers, and microfluidic applications (Squires & Quake 2005).

The dynamics of thin films either on the inside or outside of long cylinders can be modelled using the long-wave approximation, which results in the derivation of a single evolution equation for the position of the interface (Oron, Davis & Bankoff 1997; Craster & Matar 2009). Here, capillarity forces the motion of the fluid in the film and this may lead to the formation of beads in flows down the exterior of fibres (Quéré 1999; Kliakhandler, Davis & Bankoff 2001; Craster & Matar 2006; Ruyer-Quil *et al.* 2008) or the development of a liquid plug that can lead to the occlusion of a tube (Everett & Haynes 1972; Gauglitz & Radke 1988; Johnson *et al.* 1991; Newhouse & Pozrikidis 1992; Hagerdon, Martyn & Douglas 2004). The driving force behind these configurations is energy minimization through a Rayleigh mechanism. The initial stages of the flow were described by the linear stability analysis of Goren (1962), while its nonlinear evolution is determined by the equation developed by Hammond (1983), derived using lubrication theory: $h_t + (h^3[h + h_{zz}]_z)_z = 0$; here, $h(z, t)$, z and t denote the film thickness, the axial coordinate and time, respectively. In this equation, the dependence of the curvature on the film thickness was linearized consistently with the asymptotic theory, and as a result the equation can be used for situations when the film is either on the exterior or on the interior of a cylinder or fibre.

Previous work on this equation has shown that despite its apparent simplicity, it exhibits complex dynamics. This is characterized by the redistribution of the film into collars and lobes, which correspond to local equilibrium structures. The film dynamics evolve via slow drainage of the lobe into an adjacent collar (Hammond 1983; Lister *et al.* 2006); finite-time rupture of the film separating these structures is only possible via inclusion of intermolecular forces. Recent highly resolved numerical simulations by Lister *et al.* (2006) have shown that in extended domains unsteady drainage regimes are observed over exceedingly long time scales. These are punctuated by axial translation of collars leading to consumption of neighbouring lobes and the birth of new lobes in the wake of the translating collars; these are subsequently consumed when the collar slides in a reverse direction, which results in a smaller lobe being left in its wake. This motion grinds to a halt when collars collide with others that are pinned at the edges of the spatial domain by the imposed boundary conditions. Re-initiation of these episodes is possible through 'peeling' of a lobe, which occurs on longer time scales. The dynamics observed by Lister *et al.* (2006) are even more complex than those that accompany the evolution of thin films on planar surfaces governed by antagonistic intermolecular forces. In those systems, isolated droplets drift and merge on large domains over long time scales leading to coarsening to a minimum energy state (Glasner & Witelski 2003).

Over the past two decades, research in this area has explored the effect of including the full curvature in the Hammond equation in order to capture the formation of an

occluding liquid plug in a coated cylinder (Gauglitz & Radke 1988); this approach has also been complemented by full numerical simulations of the Stokes flow equations (Newhouse & Pozrikidis 1992) and of the full set of equations including surfactant effects (Campana, Di Paolo & Saita 2004). Previous studies have also accounted for a gravitationally driven motion, along the cylinder axis, and coalescence of collars and beads in flow down vertical cylinders and fibres (Quéré 1990; Tsvelodub & Trifonov 1992; Kalliadasis & Chang 1994; Quéré 1999; Chang & Demekhin 1999; Kliakhandler *et al.* 2001; Craster & Matar 2006; Ruyer-Quil *et al.* 2008). The inclusion of gravity in horizontal cylinders has also been addressed and shown to give rise to interesting instabilities that manifest themselves through periodic axial non-uniformities (Moffatt 1977; Jensen 1997; Thorodsen & Mahadevan 1997; Weidner, Schwartz & Eres 1997; Hosoi & Mahadevan 1999). Shear in core-annular flows has also been included (Aul & Olbricht 1990; Papageorgiou, Maldarelli & Rumschitzki 1990; Kerchman 1995; Joseph *et al.* 1997; Kas-Danouche, Papageorgiou & Siegel 2009) and has been shown to suppress the occurrence of capillary instabilities (Frenkel *et al.* 1987; Halpern & Grotberg 2003). Yet in spite of all the previous work carried out on thin films that coat the interior and exterior of cylinders, the effect of electrostatics and electrokinetics on the dynamics has not received much attention.

Motivated by renewed interest in electrokinetic effects, which have emerged as a key element of the physics through which fluids can be influenced, or through which separation and molecular sensing can be achieved in microfluidic devices (Squires & Quake 2005), we carefully examine the influence of electrokinetics on the deformation of thin annular fluid layers. There is interest in, amongst other applications, transverse electrokinetic pumps (Gitlin *et al.* 2003), small-scale electro-osmotic flows (Squires & Bazant 2004), and in molecular sensing using nanoporous membranes and channels (Chang & Yossifon 2009). The fluid-fluid arrangement we consider also occurs in carbon capture and storage where there is interest in how one fluid, salt-water brine, say, interacts with liquefied CO_2, in a narrow fluid-filled pore; electrokinetic effects are currently ignored in the modelling of these systems. Elucidating the effect of electrokinetics on the stability of interfaces is important in the microfluidic and carbon capture and storage applications both of which can involve the dynamics of interfaces separating electrolytic and non-electrolytic fluids. In the former set of applications, film rupture could be detrimental, while in the latter it could be beneficial, causing the entrapment of carbon dioxide.

In this paper, we consider the dynamics of an interface separating two immiscible fluids in a horizontal cylinder. The core fluid will be assumed to be perfectly conducting while the annular fluid will support the development of electrokinetic phenomena. The radial extent of the annular layer is assumed to be small in comparison to the cylinder radius and this, along with the assumption of thin dimensionless Debye layers, is used to derive a nonlinear evolution equation for the interfacial dynamics. This equation accounts for flow driven by capillarity, electrostatics and electrokinetics, and retarded by viscosity. The equation is parameterized by an electrostatic capillary number, a dimensionless inverse Debye length and the ratio of the interfacial to wall potentials. Our linear stability analysis of this equation shows that the presence of electrokinetics drives instability over an intermediate range of parameters. Our transient numerical simulations demonstrate that, over this range, finite-time film rupture occurs in a self-similar manner, with predictable scaling exponents. We note that in the absence of electrostatic and electrokinetic effects, finite-time rupture is not possible according to the model.

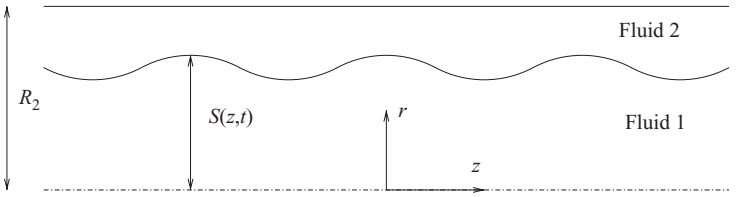

FIGURE 1. A sketch of the core-annular geometry.

The rest of the paper is organized as follows. In § 2, we provide a formulation of the interfacial problem with particular emphasis placed on the electrokinetics, the limits that extract the dominant physics and simplifications, and how they couple into the fluid mechanics. An evolution equation that represents a generalization of the Hammond equation is deduced and § 3 summarizes results from linear theory and full numerical simulations. We primarily invoke the Debye–Hückel approximation, but also perform comparative simulations using the full Poisson–Boltzmann equation. Closing remarks are provided in § 4.

2. Formulation

2.1. *Governing equations and boundary conditions*

Consider two viscous incompressible and immiscible fluids of equal densities ρ in a uniform cylindrical tube of radius R_2, and arranged in a core-annular configuration. The inner core fluid has viscosity μ_1 while the surrounding annular fluid has viscosity μ_2; a limiting case will be considered wherein the inner fluid behaves as a perfect conductor. In their undisturbed state, the fluids can be in a perfect core-annular arrangement with the core fluid a circular cylinder of radius $R_1 < R_2$ so that the interface between the two fluids is given by $r = R_1$ in a cylindrical polar coordinate system (r, θ, z). Such undisturbed states can become unstable and our objective is to describe the nonlinear spatio-temporal evolution of such two-phase systems. In general, we define the position of the interface to be $r = S(z, t)$ (the flow is assumed to be axisymmetric) and denote the regions $0 < r < S(z, t)$ and $S(z, t) < r < R_2$ by 1 and 2, respectively; the variables in each phase are distinguished by subscripts i with $i = 1, 2$. A schematic is provided in figure 1.

Electrical effects follow from the electrostatic limit of the Maxwell equations for the electric field $\boldsymbol{E}_i$ (for typical systems of interest here, magnetic effects are negligible for frequencies in the KHz range; this follows by a comparison of terms in the magnetic induction equation that shows that the induced magnetic field can be ignored even for system sizes much larger than the ones considered here) so

$$\nabla \cdot (\varepsilon_0 \varepsilon_i \boldsymbol{E}_i) = \rho_i^e, \qquad \nabla \times \boldsymbol{E}_i = 0 \tag{2.1}$$

where ε_0 is the permittivity of free space, the ε_i are the relative dielectric permittivities of each fluid and ρ_i^e is the volume charge density in each fluid. It is convenient to introduce a potential ϕ_i such that

$$\boldsymbol{E}_i = -\nabla \phi_i, \tag{2.2}$$

and the second of (2.1) is satisfied identically. Natural boundary conditions across an interface are that

$$\| \varepsilon_i \boldsymbol{E}_i \cdot \boldsymbol{n} \| = q/\epsilon_0, \qquad \| \boldsymbol{E}_i \cdot \boldsymbol{t} \| = 0 \tag{2.3}$$

where q represents any interfacial charge density, the vectors $\boldsymbol{n}, \boldsymbol{t}$ are the outward pointing unit normal vector and tangent vector at any point on the interface, and $\|(\cdot)\|$ denotes the jump in $(\cdot)$ across the interface, that is, $(\cdot)_2 - (\cdot)_1$. The charge satisfies the following conservation equation (Saville 1997):

$$q_t + \boldsymbol{u}_s \cdot \nabla_s q - q\boldsymbol{n} \cdot (\boldsymbol{n} \cdot \nabla)\boldsymbol{u}_s = \sigma_1(-\nabla \phi_1 \cdot \boldsymbol{n}) - \sigma_2(-\nabla \phi_2 \cdot \boldsymbol{n}), \tag{2.4}$$

where σ_i $(i = 1, 2)$ denote the conductivity of phase 'i' and $\boldsymbol{u}$ is the fluid velocity and the subscript s denotes that it is evaluated at the interface.

We shall assume that each electrolyte is a symmetric $z : z$ electrolyte and use the superscript $+, -$ for the cationic and ionic species $n_i^{(+)}, n_i^{(-)}$ respectively. In addition, there is a charge neutral species, with concentration n_i, from which the ionic ones disassociate. The charge density in each fluid is related to the ionic concentrations $n_i^{(\pm)}$ via

$$\rho_i^e = e\left(n_i^{(+)} - n_i^{(-)}\right) \tag{2.5}$$

where e is the charge on an electron.

The ionic concentrations evolve according to the Nernst–Planck equations

$$\frac{\mathrm{D}n_i}{\mathrm{D}t} = \nabla \cdot (\omega_i k_B T \nabla n_i) - \left(\alpha_i n_i - \beta_i n_i^{(+)} n_i^{(-)}\right), \tag{2.6}$$

$$\frac{\mathrm{D}n_i^{(\pm)}}{\mathrm{D}t} = \nabla \cdot \left(\omega_i [\pm e n_i^{(\pm)} \nabla \phi_i + k_B T \nabla n_i^{(\pm)}]\right) + \left(\alpha_i n_i - \beta_i n_i^{(+)} n_i^{(-)}\right), \tag{2.7}$$

where k_B, T and ω_i are Boltzmann's constant, absolute temperature and the mobility of the species (assumed equal for each species in each fluid), and $\mathrm{D}/\mathrm{D}t$ is the convective derivative. The reaction terms arise from a kinetic model of the disassociation and association of the ions, with rates α_i, β_i respectively (see e.g. Saville 1997).

It is useful to introduce the ionic 'velocities' $\boldsymbol{v}_i^{(\pm)}$ as

$$\boldsymbol{v}_i^{(\pm)} = \boldsymbol{u}_i - \omega_i \left[\pm e \nabla \phi_i + k_B T \nabla \log n_i^{(\pm)}\right]. \tag{2.8}$$

At the rigid surface, $r = R_2$, where the normal is in the radial direction, $\boldsymbol{n} = \boldsymbol{r}$, we have the following boundary conditions:

$$\phi_2 = \phi_w, \qquad \boldsymbol{r} \cdot \boldsymbol{v}_2^{(\pm)} = 0. \tag{2.9}$$

The latter condition can be re-expressed as

$$\boldsymbol{r} \cdot \left[\pm e \nabla \phi_i + k_B T \nabla \log n_i^{(\pm)}\right] = 0 \qquad \text{on } r = R_2. \tag{2.10}$$

At the interface between the two fluids, $r = S(z, t)$ with normal $\boldsymbol{n}$, the boundary conditions are that

$$\|\varepsilon_i \boldsymbol{n} \cdot \nabla \phi_i\| = -q/\varepsilon_0, \qquad \|\boldsymbol{t} \cdot \nabla \phi_i\| = 0, \qquad \|\boldsymbol{n} \cdot \boldsymbol{v}_i^{(\pm)}\| = 0. \tag{2.11}$$

The first two conditions represent a jump in the displacement field (Gauss's law) if interfacial charge is present and continuity of the tangential component of the electric field across the interface, where we have substituted (2.2) into (2.3); the last condition arises from integrating the ionic concentration equations across the interface. The potential at $r = 0$, the centre of the core fluid, is bounded and assumed constant $\phi_1 = \phi_I$. The potentials are arbitrary to within a constant and we fix this by assuming that there is an equilibrium state with $\phi_2 = 0$ and associated ion concentrations n_2^0.

The Navier–Stokes equations in each region govern the flow and are written as

$$\rho \frac{\mathrm{D}\boldsymbol{u}_i}{\mathrm{D}t} = \nabla \cdot \left(\boldsymbol{T}_i^f + \boldsymbol{T}_i^e\right), \qquad \nabla \cdot \boldsymbol{u}_i = 0, \tag{2.12}$$

assuming incompressibility, and where the fluid and Maxwell stress tensors appearing in (2.12) are given by

$$\boldsymbol{T}_i^f = -p_i \boldsymbol{I} + \tfrac{1}{2}\mu_i \left((\nabla \boldsymbol{u}_i) + (\nabla \boldsymbol{u}_i)^{\mathrm{T}}\right), \qquad \boldsymbol{T}_i^e = \varepsilon_i \varepsilon_0 \left(\boldsymbol{E}_i \boldsymbol{E}_i - \tfrac{1}{2}|\boldsymbol{E}_i|^2 \boldsymbol{I}\right). \tag{2.13}$$

The boundary conditions are those of no-slip and no-penetration at the tube wall $\boldsymbol{u}_2(R_2, z, t) = 0$ and boundedness of $\boldsymbol{u}_1(0, z, t)$. At the interface between regions 1 and 2 we have continuity of velocities

$$\|\boldsymbol{u}_i(S(z,t), z, t)\| = 0, \tag{2.14}$$

along with the continuity of tangential and normal stresses, the latter introducing the effects of surface tension, γ, which take the form

$$\|\boldsymbol{n} \cdot (\boldsymbol{T}^f + \boldsymbol{T}^e) \cdot \boldsymbol{t}\| = 0, \qquad \|\boldsymbol{n} \cdot (\boldsymbol{T}^f + \boldsymbol{T}^e) \cdot \boldsymbol{n}\| = \gamma \mathscr{K}, \tag{2.15}$$

where the normal and tangent vectors at a point on the interface are given by $\boldsymbol{n} = (1, -S_z)/(1 + S_z^2)^{1/2}$ and $\boldsymbol{t} = (S_z, 1)/(1 + S_z^2)^{1/2}$, respectively, and $\mathscr{K}$ is the curvature of the interface. We note that the tangential stress balance can be simplified using the fact that $\|\boldsymbol{n} \cdot \boldsymbol{T}^e \cdot \boldsymbol{t}\| = q(\boldsymbol{E} \cdot \boldsymbol{t})$. In the asymptotic analysis that follows we identify and consider the limit of a perfectly conducting core which implies that the interface is an equipotential. This implies in turn that $\boldsymbol{E} \cdot \boldsymbol{t} = 0$ so that the usual viscous flow tangential stress balance equation follows.

Finally, we have a kinematic condition at the interface which is

$$u_i = S_t + w_i S_z. \tag{2.16}$$

In solving the full problem formulated above, we take advantage of various limits that are most easily seen after a non-dimensionalization and the use of dimensionless groupings.

2.2. *Non-dimensionalization*

The mathematical model introduced in § 2.1 is made dimensionless by scaling lengths, time, velocities, pressure and voltage potentials by R_1, $(R_1\mu_1/\gamma)$, (γ/μ_1), (γ/R_1) and $(k_B T/e)$, respectively. The dimensionless velocities in regions 1 and 2 are written in component form as $\boldsymbol{u}_1 = (U, W)$ and $\boldsymbol{u}_2 = (u, w)$ and the corresponding pressures are denoted by P and p in core and film, respectively. More specifically, the non-dimensionalization is

$$(z, r, S) = R_1(\tilde{z}, \tilde{r}, \tilde{S}), \quad \phi_i = \frac{k_B T}{e}\tilde{\phi}_i, \quad \left(\boldsymbol{E}_i, \frac{q}{\varepsilon_0}\right) = \frac{k_B T}{e R_1}(\tilde{\boldsymbol{E}}_i, \tilde{q}), \quad n_i^{(\pm)} = n_2^0 \tilde{n}_i^{(\pm)}, \tag{2.17}$$

$$\rho_i^e = 2 n_2^0 e \tilde{\rho}^e, \quad \omega_i^{(\pm)} = \omega_i^0 \tilde{\omega}_i^{(\pm)}, \quad (\boldsymbol{u}_i, \boldsymbol{v}_i) = \frac{\gamma}{\mu_1}(\tilde{\boldsymbol{u}}_i, \tilde{\boldsymbol{v}}_i), \quad p_i = \frac{\gamma}{R_1}\tilde{p}_i. \tag{2.18}$$

Hereafter we work entirely in non-dimensional variables and drop the tilde decoration.

Gauss's law, the first of (2.1), in regions 1 and 2 becomes

$$\nabla^2 \phi_1 = -\chi^2 \rho_1^e \frac{\varepsilon_2}{\varepsilon_1} = -\chi^2 \frac{\varepsilon_2}{\varepsilon_1}\left(n_1^{(+)} - n_1^{(-)}\right), \tag{2.19}$$

$$\nabla^2 \phi_2 = -\chi^2 \rho_2^e = -\chi^2 \left(n_2^{(+)} - n_1^{(-)}\right). \tag{2.20}$$

The important non-dimensional group χ is the ratio of the geometry length scale R_1 to the Debye length κ,

$$\chi^2 = \frac{2R_1^2 e^2 n_2^0}{k_B T \varepsilon_2 \varepsilon_0} = \frac{R_1^2}{\kappa^2}, \qquad \left(\kappa^2 = \frac{k_B T \varepsilon_2 \varepsilon_0}{2e^2 n_2^0}\right). \tag{2.21}$$

At the wall, $r = a = R_2/R_1$, (2.9) remains unaltered:

$$\phi_2 = \phi_w, \qquad \boldsymbol{r} \cdot \boldsymbol{v}_2^{(\pm)} = 0, \tag{2.22}$$

and on the axis $r = 0$ we have $\phi_1 = \phi_I$. Non-dimensionalizing the boundary conditions (2.11) at $r = S$ yields

$$\left[\frac{\varepsilon_2}{\varepsilon_1} \nabla \phi_2 - \nabla \phi_1\right] \cdot \boldsymbol{n} = \frac{-q}{\varepsilon_1}, \qquad \phi_1 = \phi_2, \qquad \left\|\boldsymbol{n} \cdot \boldsymbol{v}_i^{(\pm)}\right\| = 0, \tag{2.23}$$

the charge equation (2.5) becomes

$$\rho_i^e = \tfrac{1}{2}\left(n_i^{(+)} - n_i^{(-)}\right), \tag{2.24}$$

and the interfacial charge conservation equation (2.4) becomes

$$q_t + \boldsymbol{u} \cdot \nabla_s q - q\boldsymbol{n} \cdot (\boldsymbol{n} \cdot \nabla)\boldsymbol{u}_s = \Sigma_1(-\nabla \phi_1 \cdot \boldsymbol{n}) - \Sigma_2(-\nabla \phi_2 \cdot \boldsymbol{n}). \tag{2.25}$$

In (2.25), $\Sigma_i \equiv \sigma_i \mu_1 / R_1 \varepsilon_0 \gamma$ represent ratios of flow to charge relaxation time scales.

The dimensionless versions of the Nernst–Planck equations (2.6) and (2.7) take the form, starting with that for the neutral species,

$$Pe_i \frac{\mathrm{D}n_i}{\mathrm{D}t} = \nabla \cdot (\omega_i \nabla n_i) - Da_i\left(n_i - K n_i^{(+)} n_i^{(-)}\right), \tag{2.26}$$

with the ionic concentrations evolving according to conservation equations

$$Pe_i \frac{\mathrm{D}n_i^{(\pm)}}{\mathrm{D}t} = \nabla \cdot \left(\omega_i \left[\pm n_i^{(\pm)} \nabla \phi_i + \nabla n_i^{(\pm)}\right]\right) + Da_i\left(n_i - K_i n_i^{(+)} n_i^{(-)}\right) \tag{2.27}$$

or equivalently

$$Pe_i \frac{\partial n_i^{(\pm)}}{\partial t} + \nabla \cdot \left(n_i^{(\pm)} \boldsymbol{v}_i^{(\pm)}\right) = Da_i\left(n_i - K_i n_i^{(+)} n_i^{(-)}\right), \tag{2.28}$$

where the non-dimensional ion velocities are

$$\boldsymbol{v}_i^{(\pm)} = Pe_i \boldsymbol{u}_i - \omega_i\left[\pm \nabla \phi_i + \nabla \log n_i^{(\pm)}\right]. \tag{2.29}$$

The dimensionless groups appearing above are the Péclet and Damköhler numbers given by

$$Pe_i = \frac{\gamma R_1}{\omega_i^0 k_B T \mu_1}, \qquad Da_i = \frac{R_1^2 \alpha_i}{k_B T \omega_i^0}, \tag{2.30}$$

which represent the ratio of flow to diffusional (due to charge) velocity scales and the ratio of diffusion to reaction time scales, respectively. In the reaction terms, we also have the ratio of disassociation to association rates

$$K_i = \beta_i n_2^0 / \alpha_i. \tag{2.31}$$

The dimensionless Navier–Stokes equations become

$$J\,(u_{it} + u_i u_{ir} + w_i u_{iz}) = -p_{ir} - Q\chi^2 \rho_i^e \phi_{ir} + m_i\left(\nabla^2 u_i - \frac{1}{r^2} u_i\right), \tag{2.32}$$

$$J\left(w_{it}+u_i w_{ir}+w_i w_{iz}\right)=-p_{iz}-Q\chi^2\rho_i^e\phi_{iz}+m_i\nabla^2 w_i, \tag{2.33}$$

$$\frac{1}{r}(ru_i)_r+w_{iz}=0, \tag{2.34}$$

where $\nabla^2\equiv\partial^2/\partial r^2+(1/r)\partial/\partial r+\partial^2/\partial z^2$ with $m_1=1$ and $m_2=\mu_2/\mu_1=m$, the latter representing the annulus to core fluid viscosity ratio. The dimensionless parameters appearing in (2.32) and (2.33) are

$$J=\frac{\rho\gamma R_1}{\mu_1^2},\qquad Q=\frac{\varepsilon_2\varepsilon_0(kT/e)^2}{\gamma R_1}, \tag{2.35}$$

which represent a surface tension parameter J introduced by Chandrasekhar (1961), and an electric Weber number Q which is the ratio of electrostatic to capillary pressures; the dimensionless inverse Debye length parameter χ^2 has been defined in (2.21).

The interfacial conditions of tangential and normal stress balances become

$$m\left[(u_z+w_r)\left(1-S_z^2\right)+2u_rS_z-2w_zS_z\right]=(U_z+W_r)\left(1-S_z^2\right)+2U_rS_z-2W_zS_z, \tag{2.36}$$

$$\begin{aligned}p\left(1+S_z^2\right)-2mu_r-2mw_zS_z^2+2m(u_z+w_r)S_z-\left[P\left(1+S_z^2\right)-2U_r-2W_zS_z^2+2(U_z+W_r)S_z\right]\\ -Q\left[\frac{1}{2}\left(1-S_z^2\right)\left(\phi_{2r}^2-\phi_{2z}^2\right)-2S_z\phi_{2r}\phi_{2z}\right]+Q\frac{\varepsilon_1}{\varepsilon_2}\left[\frac{1}{2}\left(1-S_z^2\right)\left(\phi_{1r}^2-\phi_{1z}^2\right)-2S_z\phi_{1r}\phi_{1z}\right]\\ =\left[S_{zz}-\frac{1+S_z^2}{S}\right]\left(1+S_z^2\right)^{-1/2},\end{aligned} \tag{2.37}$$

while the kinematic condition (2.16) retains its form. Finally, we have continuity of velocities at $r=S(z,t)$, no-slip and no-penetration conditions at the wall, and boundedness of velocities at $r=0$.

2.3. *The thin annulus limit*

We proceed by assuming that the dimensionless undisturbed annular thickness is small, that is $(R_2-R_1)/R_1\equiv\epsilon\ll 1$ (this is a useful limit in practice; see Wei & Rumschitzki 2002). This implies that the tube wall has a dimensionless radius

$$a=1+\epsilon. \tag{2.38}$$

The interface is perturbed about its dimensionless uniform state, with an amplitude that scales with the annulus thickness, so that its position is

$$S=1+\epsilon H(z,t), \tag{2.39}$$

with $H(z,t)$ to be found. It is convenient to introduce a stretched variable y to describe region 2, given by

$$r=1+\epsilon-\epsilon y. \tag{2.40}$$

In terms of y, the tube wall is at $y=0$ while the interface is at $y=1-H(z,t)$. The flows under consideration are driven by electric fields and capillary forces, and in the asymptotic models sought here we retain both physical effects. The magnitude of the pressure is set by balancing the film pressure p with the capillary pressure in the normal stress balance (2.37). For interfacial perturbations (2.39) the perturbation capillary pressure is of the order of ϵ and hence we have $p-\overline{p}_0\sim\epsilon$ where $\overline{p}_0$ is the

constant unperturbed value. It follows that the perturbation axial velocity from (2.33) is of the order of ϵ^3 and the corresponding radial velocity is of the order of ϵ^4 as follows by (2.34). Finally, the electric stress term in (2.37) has size Q/ϵ^2 (assuming that $\phi = O(1)$) and thus we require $Q \sim \epsilon^3$ to make the electrostatic effect compete with surface tension – if $Q \gg \epsilon^3$ then surface tension does not enter. Finally, continuity of velocities at the interface induces a flow $(U, W) \sim \epsilon^3$ in the core, which in turn induces a pressure perturbation $P - \overline{P}_0 \sim \epsilon^3$ because the core region is characterized by order-one radial and axial coordinates without a lubrication-type flow governing the dynamics. The appropriate asymptotic expansions in film and core are, then,

$$u = \epsilon^4 u_{(1)} + \epsilon^5 u_{(2)} + \cdots, \quad w = \epsilon^3 w_{(1)} + \epsilon^4 w_{(2)} + \cdots, \quad p = \overline{p}_{(0)} + \epsilon p_{(1)} + \cdots, \tag{2.41}$$

$$(U, W) = \epsilon^3 (U_{(1)}, W_{(1)}) + \epsilon^4 (U_{(2)}, W_{(2)}) + \cdots, \quad P = \overline{P}_{(0)} + \epsilon^3 P_{(1)} + \cdots. \tag{2.42}$$

An inspection of the momentum equations (2.32) and (2.33) shows that the electrokinetic effects will enter to leading order if $Q\chi^2 \sim \epsilon$, which along with the scaling found for Q implies the canonical limit

$$Q = \epsilon^3 \overline{Q}, \qquad \chi^2 = \frac{1}{\epsilon^2} \overline{\chi}^2. \tag{2.43}$$

The latter estimate, coupled with the definition (2.21) for the Debye length, shows that we are analysing cases when the dimensionless Debye length $1/\chi$ is of the order of ϵ, that is it is of the same order as the annular film thickness. We have also assumed the viscosity ratio to be of order one.

We are mainly concerned with the dynamics in the film and in particular the effect of ion mobility on interfacial instabilities. To this end, we concentrate on regimes where electrokinetic effects in the core are negligible compared with those in the film (see also Georgiou *et al.* 1991). We see from the Debye length scale (2.43) that the charge density in the core on the right-hand side of (2.19) is of the order of $(\varepsilon_2/\varepsilon_1)\epsilon^{-2}$, implying the ordering $(\varepsilon_2/\varepsilon_1) \ll \epsilon^2$ for electrokinetic effects to be absent and hence leading to $\nabla^2 \phi_1 = 0$ to leading order. One way to achieve this is to take the distinguished limit $(\varepsilon_2/\varepsilon_1) \sim \epsilon^3$, for example, and this is sufficient for our purposes.

This limit also influences the boundary condition (2.23) with $\boldsymbol{n} \cdot \nabla \phi_1 = q/\varepsilon_1$ to leading order. The substitution of this result into (2.25) and assuming the core fluid to be highly conducting, that is, $\Sigma_1 \gg 1$, yields $(\Sigma_1/\varepsilon_1)q \approx 0$. The leading-order boundary condition given by (2.23) then gives $\boldsymbol{n} \cdot \nabla \phi_1 \approx 0$, thereby decoupling the potential field in the core from that of the wall fluid. Assuming that the core fluid is drawn from a charge-neutral reservoir of fixed potential ϕ_I, the potential will be constant and equal to ϕ_I throughout region 1. In this case, the electric field problem in the film is closed and the Gauss law (2.24) is an identity for the local charge concentration at the interface and is not needed in the analysis that follows (we note in passing that if the core and film electric field problems are coupled, the Gauss law is required and the value of q in (2.23) is determined from the charge conservation equation (2.25) – this is the so-called leaky dielectric model). Furthermore, the ionic concentrations are constant in the core and the ionic velocity zero. In this case, the first two boundary conditions (2.23) are replaced by

$$\phi_2 = \Phi_I \qquad \text{on } \; y = 1 - H(z, t), \tag{2.44}$$

which states that the interface is an equipotential surface. This closes the film problem as far as the electric field problem is concerned but hydrodynamic coupling cannot be ruled out – it turns out, as we will see below, that in the thin annular limit

with order-one viscosity ratios hydrodynamic coupling between film and core is also absent.

The electrokinetic effects in the film are considered in the distinguished limit of $(Pe_i, Da_i) \sim O(1)$ and the Nernst–Planck equations (2.27) reduce to (note that radial derivatives dominate in the film)

$$\left[\omega_2 n_2^{(\pm)}\left[\pm\phi_2 + \log n_2^{(\pm)}\right]_y\right]_y = \left[n_2^{\pm} v_{2(y)}^{(\pm)}\right]_y = 0 \tag{2.45}$$

with $v_{2(y)}$ denoting the y component of the ionic velocity. In this limit the ionic concentrations instantaneously adjust to the potential and $n_2^{(\pm)}$ are enslaved to the potentials ϕ_2. The precise dependence of $n_2^{(\pm)}$ on ϕ_2 determines the equation for ϕ_2 when the ion concentrations are substituted into (2.20) (for example the classical Poisson–Boltzmann equation which we encounter below).

The boundary conditions on $v_{2(y)}$ to leading order are that it is zero at both the wall and interface. Integration of (2.45) and use of the boundary conditions yields

$$\pm\phi_2 + \log n_2^{(\pm)} = \text{constant} \quad \rightarrow \quad n_2^{(\pm)} = K_{\pm}\exp(\mp\phi_2), \tag{2.46}$$

where $K_{\pm}$ are constants. For the given electrolyte we assume that there exists an electro-neutral state at a dimensionless potential ϕ_0, say. The number density of positive and negative ions is then equal to a neutral-state value n_2^0, which is also the value used in the non-dimensionalizations (2.17). Using the solutions (2.46) gives

$$K_+\exp(-\phi_0) = K_-\exp(\phi_0) = n_2^0, \tag{2.47}$$

which in turn yields

$$n^{(+)} - n^{(-)} = 2K_+\exp(-\phi_0)\sinh(\phi_0 - \phi) = 2n_2^0\sinh(\phi_0 - \phi). \tag{2.48}$$

Noting the non-dimensionalizations and making use of the stretched coordinate (2.40) and the scaling (2.43), one can use Gauss's law (2.20) to express the Poisson–Boltzmann equation as follows:

$$\frac{1}{\epsilon^2}\phi_{2yy} - \frac{1}{1+\epsilon-\epsilon y}\phi_{2y} + \phi_{2zz} = \frac{1}{\epsilon^2}\overline{\chi}^2\sinh(\phi - \phi_0). \tag{2.49}$$

We emphasize that without loss of generality the reference potential ϕ_0 can be set to zero. We seek a solution in the form of an asymptotic expansion:

$$\phi_2(y, z, t) = \phi(y, z, t) + \epsilon\phi_{(1)}(y, z, t) + \cdots. \tag{2.50}$$

This gives to leading order

$$\phi_{yy} = \overline{\chi}^2\sinh\phi, \tag{2.51}$$

which must be solved subject to the wall and interface boundary conditions

$$\phi(0, z, t) = \phi_w, \qquad \phi(1 - H(z, t), z, t) = \phi_I. \tag{2.52}$$

Given the potential distribution, the ionic concentrations follow immediately from (2.46). It is commonplace to invoke a further approximation, the Debye–Hückel limit, with $\phi \ll 1$ so that (2.51) becomes $\phi_{yy} = \overline{\chi}^2\phi$ (this limit is appropriate as long as the potential in the layer is close to the charge neutrality value ϕ_0, that is $|\phi - \phi_0| \ll 1$, recalling that the choice $\phi_0 = 0$ has been made). This has the advantage that simple analytic solutions emerge and we distinguish these with a superscript DH. Numerical solutions or a formal analytic expression involving elliptic functions can be deduced for the general case. The linearized Poisson–Boltzmann equation subject

to the boundary conditions (2.52) yields

$$\phi^{DH}(y,z,t) = \phi_W \cosh\overline{\chi}y + \left(\frac{\phi_I - \phi_W \cosh\overline{\chi}(1-H)}{\sinh\overline{\chi}(1-H)}\right)\sinh\overline{\chi}y. \tag{2.53}$$

Using the expansions (2.41) and (2.42) in the normal stress balance equation (2.37) gives to leading order

$$p_{(1)}|_{(1-H)} = \tfrac{1}{2}\overline{Q}\,\phi_y^2\big|_{(1-H)} + H + H_{zz}. \tag{2.54}$$

The leading-order radial momentum equation becomes

$$p_{(1)y} - \overline{Q}\overline{\chi}^2\phi_y \sinh\phi = 0, \tag{2.55}$$

which can be integrated to give

$$p_{(1)}(y,z,t) = \overline{Q}\overline{\chi}^2\cosh^2\phi(y,z,t) + K(z,t), \tag{2.56}$$

where the function $K(z,t)$ is determined by substituting the boundary value (2.54) into the solution (2.56). The result is

$$K(z,t) = \tfrac{1}{2}\overline{Q}\left[\phi_y^2|_{1-H} - 2\overline{\chi}^2\cosh\phi\right] + H + H_{zz}, \tag{2.57}$$

with the limiting Debye–Hückel case obtainable in terms of $H(z,t)$ as follows:

$$K^{DH}(z,t) = \frac{1}{2}\overline{Q}\overline{\chi}^2\left[\left(\frac{\phi_W - \phi_I\cosh\overline{\chi}(1-H)}{\sinh\overline{\chi}(1-H)}\right)^2 - \phi_I^2\right] + H + H_{zz}. \tag{2.58}$$

An evolution equation is obtained from the kinematic condition (2.16) once the leading-order film velocities are determined. The leading-order lubrication balance in (2.33) enables us to find $w_{(1)}$ in the form

$$w_{(1)}(y,z,t) = \frac{y^2}{2m}K_z(z,t) + yL(z,t) + M(z,t), \tag{2.59}$$

which on using the no-slip condition $w_{(1)}(0,z,t)=0$ at the wall along with the leading-order tangential stress balance,

$$w_{(1)y}(1-H,z,t) = 0, \tag{2.60}$$

gives

$$w_{(1)}(y,z,t) = \frac{1}{m}\left[\frac{1}{2}y^2 - (1-H)y\right]K_z(z,t). \tag{2.61}$$

Continuity then provides the corresponding radial velocity:

$$u_{(1)}(y,z,t) = \frac{y^3}{6m}K_{zz} - \frac{y^2}{2m}(1-H)K_{zz} + \frac{y^2}{2m}H_zK_z. \tag{2.62}$$

Substituting (2.61) and (2.62) into the kinematic condition (2.16) and introducing a new slow time scale by $\partial/\partial t \to (1/3m)\epsilon^3\partial/\partial t$ produces the following evolution equations:

$$H_t + \left[(1-H)^3K_z\right]_z = 0, \qquad K_z = H_z + H_{zzz} + \frac{1}{2}\overline{Q}\frac{\partial}{\partial z}\left(\phi_y|_{1-H}\right)^2, \tag{2.63}$$

$$K_z^{DH} = H_z + H_{zzz} + \frac{1}{2}\overline{Q}\overline{\chi}^2\frac{\partial}{\partial z}\left(\frac{\phi_W - \phi_I\cosh\overline{\chi}(1-H)}{\sinh\overline{\chi}(1-H)}\right)^2. \tag{2.64}$$

In the numerical work that follows, we prefer to introduce a new dependent variable

$$\eta(z,t) = 1 - H(z,t), \tag{2.65}$$

which represents the dimensionless film thickness so that $\eta = 0$ corresponds to solutions which touch the solid wall. In terms of η, the equation becomes

$$\eta_t + \left[\eta^3(\eta_z + \eta_{zzz}) - \frac{1}{2}\overline{Q}\eta^3\left\{\phi_y^2|_\eta\right\}_z\right]_z = 0, \tag{2.66}$$

with the Debye–Hückel version as

$$\eta_t^{DH} + \left[\eta^{DH3}\left(\eta_z^{DH} + \eta_{zzz}^{DH}\right) - \frac{1}{2}\hat{Q}\overline{\chi}^2\eta^{DH3}\left\{\left(\frac{1 - \Phi\cosh\overline{\chi}\eta^{DH}}{\sinh\overline{\chi}\eta^{DH}}\right)^2\right\}_z\right]_z = 0, \tag{2.67}$$

where

$$\Phi = \phi_I/\phi_W, \qquad \hat{Q} = \overline{Q}\phi_W^2. \tag{2.68}$$

This conveniently embeds the wall potential in $\hat{Q}$. So for the Debye–Hückel limit there are now three parameters $\hat{Q}, \overline{\chi}$ and Φ. The equation is to be solved with appropriate initial conditions about the undisturbed position $\eta = 1$ and periodic boundary conditions in z.

In summary, the interfacial dynamics are governed by (2.66) or (2.67) depending on whether the Debye–Hückel limit is invoked or not. The former is coupled to the Poisson–Boltzmann equation (2.51) for the potential in the film, ϕ. The latter was derived by first linearizing (2.51) to obtain the Debye–Hückel equation; this is permissible when the magnitude of the potential is relatively small. Both evolution equations, which have been derived in the thin-annulus limit and for cases wherein the electric permittivity of the bulk far exceeds that of the film, are parameterized by three dimensionless groups: Φ represents the ratio of the interfacial to the wall potential, $\overline{Q}$ is a rescaled electrostatic capillary number, and $\bar{\chi}$ is a rescaled inverse Debye length (large values of this parameter correspond to thin electric double layers and *vice versa*). Furthermore, we have considered situations in which the Debye length is of the same order as the thickness of the film, and the magnitude of electrostatic effects is relatively small; this was done in order to balance electrokinetics and electrostatics with capillary effects. Finally, although the solutions of (2.67) will primarily be discussed below, it is important to note the limitations of the Debye–Hückel approximation whose validity may become questionable if electro-neutrality does not hold over a region in the film; such situations will arise when electric double layers scale with the film thickness (Chang & Yeo 2010).

3. Results

3.1. *Limiting cases and linear stability*

In the absence of an electric field ($\overline{Q} = 0$), the evolution equation reduces to that derived and studied by Hammond (1983). Hammond finds that the capillary forces drive the interface towards the wall but it never actually touches the wall; instead the flow evolves into a quasi-static configuration of 'lobes' and 'collars'. An extensive study by Lister *et al.* (2006) has established some intricate dynamics at very long times, including the spontaneous axial translation of a lobe up and down the cylinder. Our model equation (2.66), therefore, contains additional physical effects that modify Hammond-type dynamics significantly because they lead to finite-time wall touchdown

of the interface, as will be shown below. It is also found that some novel non-uniform stable steady states are also possible at sufficiently large values of the parameter $\overline{\chi}$, establishing that electrokinetic effects act as a nonlinear saturation mechanism.

The absence of electrokinetics provides another limit that corresponds to the dynamics of a dielectric film that surrounds a perfectly conducting core fluid so that there is a constant voltage drop between fluid–fluid interface and the cylinder wall. This case has been derived and studied by Wang (2009) and arises from (2.66) and (2.67) in the limit $\overline{\chi}\eta \to 0$; the electrostatic equation becomes

$$\eta_t + \left[\eta^3(\eta_z + \eta_{zzz}) + \beta\eta_z\right]_z = 0, \tag{3.1}$$

where $\beta = \hat{Q}(1-\Phi)^2 > 0$ (notably the approach to this limiting equation is valid for both the nonlinear and linearized Poisson–Boltzmann equations). It has been shown in Wang (2009) that spatially periodic solutions of (3.1) starting from rather general initial conditions, terminate in self-similar finite-time touchdown singularities in contrast to the Hammond equation ($\hat{Q} = 0$). An extension of these results to non-zero values of $\overline{\chi}$ is carried out in the present study. In addition, Wang (2009) performed boundary integral simulations and verified the touchdown dynamics supported by the thin film electrostatic system.

The linear stability of the general equation (2.66) is studied by writing $\eta = 1 + \hat{\eta}\exp(ikz + st)$ and linearizing with respect to $\hat{\eta}$. The dispersion relation is

$$s(k) = k^2\left(1 - \frac{\overline{Q}}{2}\frac{\partial\phi_y^2}{\partial\eta}\Big|_{\eta=1} - k^2\right), \tag{3.2}$$

which in the Debye–Hückel limit becomes explicit as

$$s^{DH}(k) = k^2\left(1 - \hat{Q}\lambda(\overline{\chi}) - k^2\right), \qquad \lambda(\overline{\chi}) = \frac{\overline{\chi}^3(\Phi\cosh\overline{\chi} - 1)(\cosh\overline{\chi} - \Phi)}{\sinh^3\overline{\chi}}. \tag{3.3}$$

Instability is only possible if $\hat{Q}\lambda(\overline{\chi}) < 1$ and because $\lambda \to -(1-\Phi)^2 < 0$ as $\overline{\chi} \to 0$ we confirm that small values of $\overline{\chi}$ will make the flow linearly unstable (in the limit, the results of Wang (2009) show that finite-time touchdown takes place, but such conclusions can only be drawn from nonlinear studies). The function λ is shown in figure 2 for varying Φ and has a clear (positive) maximum suggesting that there can be regions of $\overline{\chi}$ that stabilize the flow linearly; the width of these regions depends on $\hat{Q}$ and Φ. The maximal growth rate versus $\overline{\chi}$ (figure 2*c*,*d*) illustrates this; for all cases presented having $\Phi \neq 0$ we observe windows of stability for a range of $\overline{\chi}$. The size of the stability windows increases as Φ increases as confirmed by the results at two different values of $\hat{Q} = 1, 2$. The linear results presented in figure 2 have been calculated in the Debye–Hückel limit; calculations with the full model give results that are almost indistinguishable and are therefore not shown. It is worth noting that increasing ϕ_i/ϕ_w substantially eventually leads to situations in which the potential across the layer is quantitatively different, but qualitatively similar. Figure 3 shows results for $\phi_i/\phi_w = 5$, notably the growth rates differ substantially, but the trends are unchanged.

To interpret why the model gives an unstable region, followed by stability then by instability, with varying Φ, we turn to the profiles of the potential ϕ shown in figure 4 (in the Debye–Hückel limit, this potential is given by (2.53) with $H \equiv 0$). For $\Phi = 0$ (that is for zero potential at the interface, $\phi_I = 0$) the system is always unstable (see figure 2*a*) and there is a monotonically decreasing electric field (recall that the electric field in the radial direction is $-\phi_y$) across the layer for the range of values $1 \leqslant \overline{\chi} \leqslant 10$

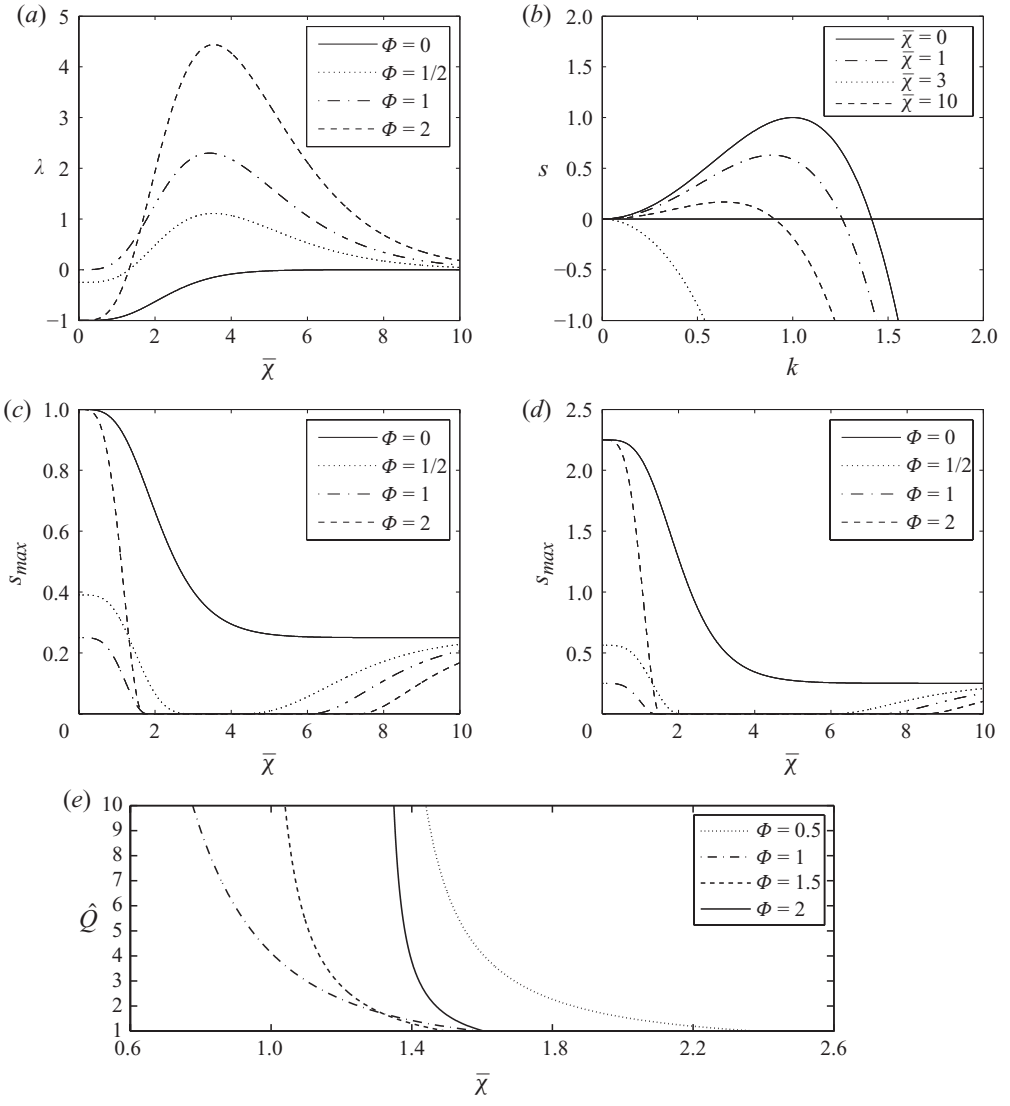

FIGURE 2. Linear stability: (*a*) the function λ versus $\overline{\chi}$; (*b*) typical dispersion curves, note the non-monotonic behaviour with respect to $\overline{\chi}$ ($\hat{Q}=1, \Phi=2$); (*c*, *d*) the maximal growth rate versus $\overline{\chi}$ for varying Φ and $\hat{Q}=1, 2$ in (*c*) and (*d*), respectively. (*e*) The solution to (3.3) with the growth rate, $s=0$, showing the critical $\bar{\chi}$ for stability at $k=0.5$.

as seen in figure 4(*a*). At values of $\overline{\chi}$ smaller than approximately 1, the electric field is almost constant as evidenced by the linear variation of the potential across the layer, while at larger values (e.g. $\overline{\chi}=10$) the field decreases rapidly to zero outside the Debye layer which is relatively small in this case. As Φ (equivalently ϕ_I) increases, this monotonic decreasing behaviour of the potential across the layer persists if Φ_I and $\overline{\chi}$ are sufficiently small, as can be seen from the results of figure 4(*b*) which correspond to a value of $\phi_I=1/2$ and show that for $\overline{\chi}$ approximately less than unity the electric field is almost constant. These are cases in which the Debye layer thicknesses are of the same order as the annular layer thickness, and there is an effective electrostatic

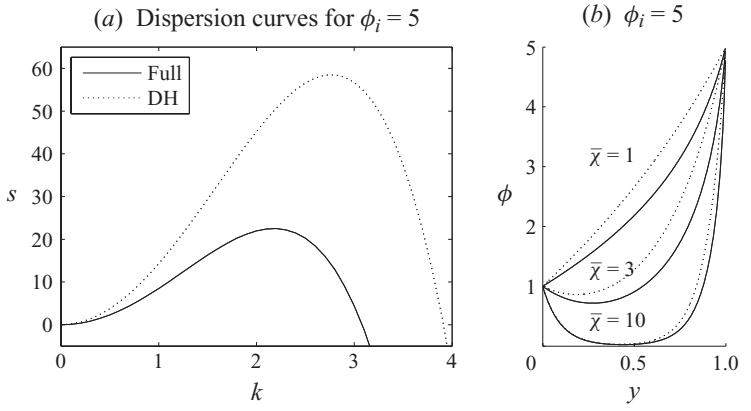

FIGURE 3. A comparison of the full Poisson–Boltzmann versus the Debye–Hückel model for $\phi_i = 5, \phi_w = 1$. (*a*) The dispersion curves for $\overline{\chi} = 1$ and (*b*) the potential across the fluid layer for $\overline{\chi} = 1$, 3 and 10.

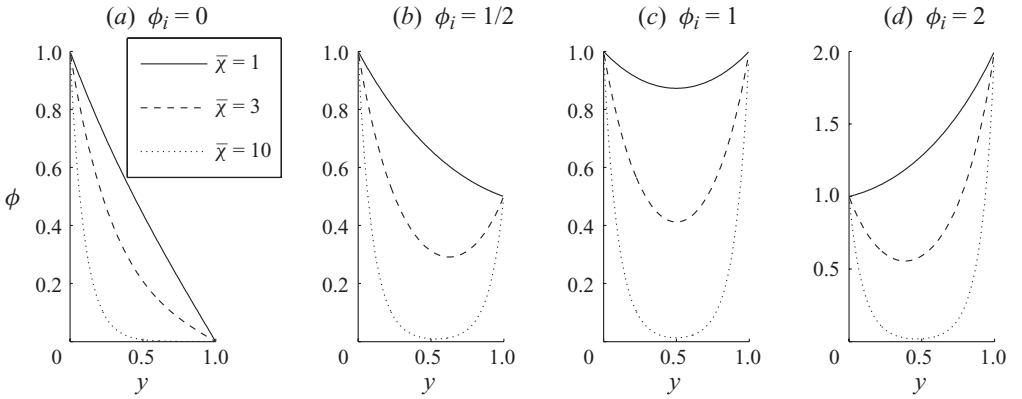

FIGURE 4. The potential across the fluid layer for $\phi_w = 1$ and ϕ_i varying from 0, 1/2, 1 to 2 for $\overline{\chi} = 1$, 3, 10.

pressure pulling the interface towards the wall causing instability. At larger values of $\overline{\chi}$, however, the electric field attains high positive values at the wall ($y = 0$) and decreases to relatively large negative values at the interface, the effect being more pronounced as $\overline{\chi}$ increases. For interface potentials 1/2, 1, 2 in figure 4(*b–d*) and large values of $\overline{\chi}$, the Debye layer thickness is much smaller than the annular layer thickness and electrical double layers form at both the wall and interface. For the value $\overline{\chi} = 3$, these double layers are sufficiently close that they interact and repel each other acting to stabilize the system. These effects maybe of relevance to separation technology involving the use of nanoporous membranes and nanochannels (Chang & Yeo 2010) where the electric double layers are no longer thin as compared to the dimensions of the channel and overlap with one another. Increasing $\overline{\chi}$ further to values $\overline{\chi} = 10$ for example leads to very narrow weakly interacting double layers and their effect on stability is weak.

These stability mechanisms can be observed in figure 2(*b*), which shows growth rate curves as $\overline{\chi}$ increases for the case $\Phi = 2$. When $\overline{\chi} = 0$, the usual capillary instability is active. As $\overline{\chi}$ increases to a value of 1, double layers form and interact by pushing the

interface away from the wall, leading to a partial stabilization seen as a decrease of both the maximum growth rate and the band of unstable waves. A further increase to $\overline{\chi} = 3$ leads to a complete linear stabilization – the interaction of the double layers is optimal in the sense that sufficiently large repulsive forces are generated to completely stabilize capillary instability. As $\overline{\chi}$ is increased further to a value of 10, the growth rate increases and the flow becomes unstable again. The double layers in this case are concentrated at the wall and interface and their stabilizing effect is significantly reduced.

The discussion above was based on linear aspects of the dynamics and we turn next to the solution of the nonlinear problem in order to quantify the physical observations afforded by linear theory.

3.2. *Numerical solution of the evolution equations*

The evolution equations (2.66) and (2.67) for the film thickness were solved numerically using three different methods, which served as a means of comparison given the highly nonlinear nature of the equations. All methods employ the method of lines with a solver designed for stiff problems (e.g. Gear's method). The first scheme used is EPDCOL (Keast & Muir 1991), which is based on a finite-element discretization in space. The second scheme is a spectral method, which uses fast Fourier transforms in space and backwards Gear for time. The final scheme uses a finite-volume method for space. The last method has the advantage of behaving better near discontinuities, which occur in the region of film rupture. Unless indicated otherwise, we mainly present results using (2.67), which is in the Debye–Hückel limit.

In a typical simulation, 2×10^3 grid points were used and the computations were stopped when the film height was within 10^{-5} dimensionless units from the wall. Numerical solutions of (2.67) were obtained on a finite domain $-L \leqslant z \leqslant L$, with $L = \pi$ or 2π typically used, and subject to periodic boundary conditions. Larger domains with $L = 5\pi$ have been investigated in order to discuss the impact of electrokinetics on the axial translation of collars observed by Lister *et al.* (2006). Because of the existence of a finite-time touchdown and steady-state solutions, we do not observe axial translation of collars. In addition, the results yield qualitatively similar information to a shorter domain, so we focus on those here. Furthermore, the film evolution was initiated by perturbing the film height as $\eta(z, 0) = 1 - A\cos(\pi z/L)$ with $A = 0.1$. For each of our computations, we have checked that the total volume of fluid in the film is conserved. As an additional check we compared our solutions against linear theory and found them to be in excellent agreement near $\eta = 1$.

The full Poisson–Boltzmann model gives results qualitatively in agreement and some comparative computations will be shown below. This full model requires the computational schemes above to be augmented with the nonlinear Poisson–Boltzmann equation (2.51) solved across the fluid layer at each grid point. The coupling to the evolution equation is via the potential gradient at the interface. Computations with the full model are numerically intensive and (2.51) is solved iteratively as a two-point boundary value problem using upto 2000 points across the layer. The iterative scheme rapidly converges, yielding the potential gradient at the interface.

In figure 5, we plot representative final film profiles as the parameters $\bar{\chi}$, $\hat{Q}$ and Φ vary. All parameters are chosen so that the corresponding linear solutions are unstable as can be confirmed by the results of figure 2 (cases which correspond to linearly stable solutions and which have moderate initial amplitudes are trivial in the sense that they lead to uniform flat film states at large times). In particular, we compute with values that correspond to both situations in which the film is capillary

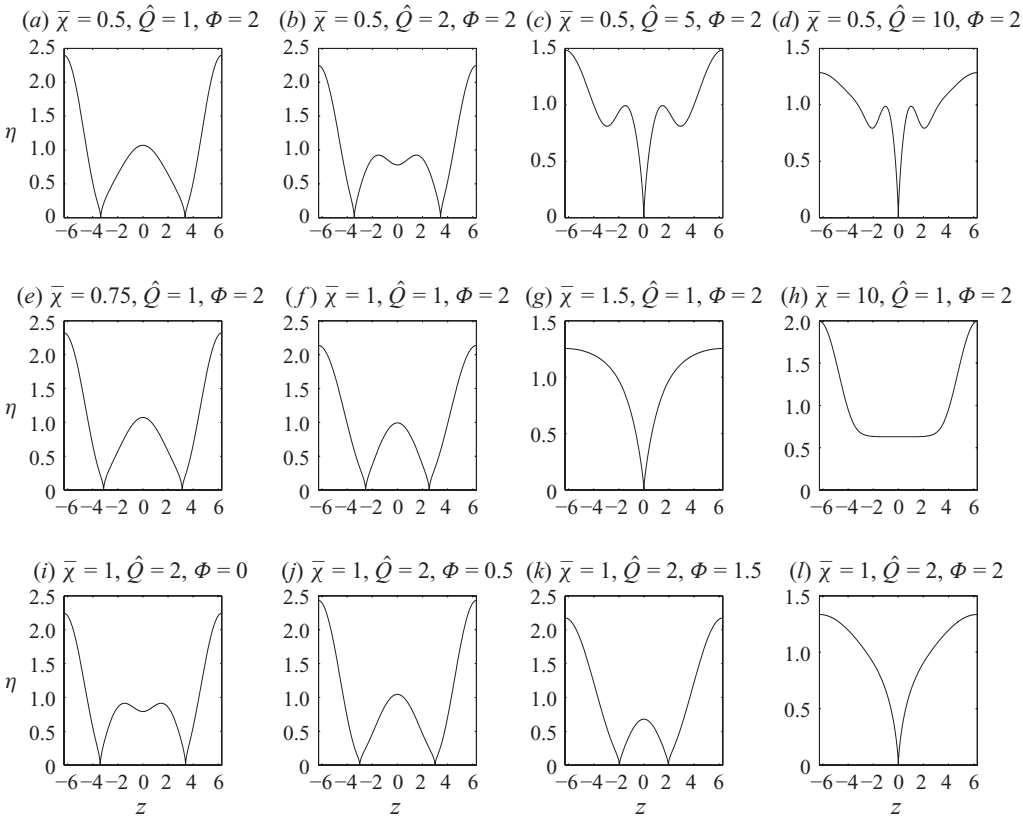

FIGURE 5. Final film profiles for the film as a function of the parameters $\bar{\chi}$, $\hat{Q}$ and Φ. Top row has fixed Φ ($\Phi = 2$), the next fixed $\hat{Q}$ ($\hat{Q} = 1$) and the final row has fixed $\bar{\chi}$ ($\bar{\chi} = 1$). The initial film height is $\eta = 1 - A\cos(\pi z/L)$, where $L = 2\pi$ and $A = 0.1$.

unstable at relatively small values of $\bar{\chi}$, and other values in which it is unstable at large values of $\bar{\chi}$ when the Debye layer thicknesses are small and confined to the vicinity of the wall and interface (these regions can be identified in figure 2*c,d* for example). More specifically, all results in figure 5 correspond to the small $\bar{\chi}$ instability island except those in figure 5(*h*) which have $\bar{\chi} = 10$ and correspond to second instability island as seen in figure 2(*d*) for example. This difference is quite important as we show below, because our results indicate that even though linear theory predicts instability, the ultimate nonlinear regime supports stable non-uniform steady states. The computations shown in this case are for the Debye–Hückel limit, and a qualitatively similar behaviour occurs for the full Poisson–Boltzmann's case.

For suitably chosen parameters, then, the film touches the wall in finite time, in contrast to the case studied by Hammond (1983) in which electrokinetics are absent and the numerical evidence suggests that the film can approach the wall only in infinite time. In that case, $\hat{Q} = 0$, capillary forces cause perturbations to grow in time and drive the formation of 'collars'. For small values of $\hat{Q}$, the initial stage of the film evolution is similar to that described by the Hammond equation, but when the film approaches the wall, the electrostatic pressure increases and causes a ring-like rupture because touchdown occurs simultaneously at two points on the tube wall; see figure 5(*a*) for instance. This touchdown behaviour is similar to that observed

by Vaynblat, Lister & Witelski (2001) when van der Waals forces are included in the model rather than electric fields. As $\hat{Q}$ is increased further, electrostatic forces become more dominant and lead to rupture of the film at the origin of the domain (see figure 5*c*,*d*); this will be referred to below as 'line rupture' because touchdown takes place at a single value of z. In the results in figure 5(*a*–*d*) we fix $\bar{\chi} = 0.5$, $\Phi = 2$ and vary the electric field strength parameter $\hat{Q}$. Linear theory predicts instability for these values and in fact increasingly larger maximum growth rates as $\hat{Q}$ is raised. The nonlinear results predict finite-time touchdown in this case with $\hat{Q}$ controlling the ultimate topology of the final state.

The second row of results (figure 5*e*–*h*) fix $\hat{Q} = 1$, $\Phi = 2$ and present final profiles as $\bar{\chi}$ is varied. In figure 5(*e*,*f*), a similar behaviour occurs with a ring rupture occurring for values of $\bar{\chi}$ smaller than one approximately (recall that $\bar{\chi}$ is the scaled ratio of geometric to Debye length scales). As the magnitude of this parameter increases, the radius of the ring decreases (equivalently, the axial distance between touchdown points decreases) and beyond a critical value of $\bar{\chi}$, line rupture emerges instead (see figure 5*g*). For larger values of $\bar{\chi}$, an electric double layer forms, stabilizing the film as shown in figure 2. The critical value of $\bar{\chi}$ that stabilizes the film is found by solving (3.3) with $s = 0$. For values of $\bar{\chi}$ below the critical value, the film is unstable and rupture in finite time always occurs. Near the critical point, λ increases with $\bar{\chi}$ as shown in figure 2(*e*); therefore the critical point, found from the solution to $\hat{Q}\lambda = 1 - k^2$, decreases as $\hat{Q}$ increases. For relatively large values of $\bar{\chi}$, the double layers are confined to the near-wall and near-interface regions, and one would expect the film to be unstable, leading to rupture; this is based on the results of the linear stability analysis presented above. In the nonlinear regime, however, as the film thins, the double layers interact and this gives rise to the steady-state profile presented in figure 5(*h*).

The last row of results (figure 5*i*–*l*) fixes $\bar{\chi} = 1$, $\hat{Q} = 2$ and varies the parameter Φ that represents the potential difference between the film interface and the wall. We see that a ring rupture event occurs for small values of Φ; see figure 5(*i*–*k*) corresponding to $\Phi = 0, 0.5, 1.5$. As Φ increases, the rupture points move closer and as seen in figure 5(*l*) a line rupture occurs at $\Phi = 2$ (and at higher values of Φ, in fact). For the parameter values of the third row of results, linear theory predicts instability for all values of Φ as readily seen from the results of figure 2(*d*). Once again, the value of Φ can be used to control the topology of the ultimate touchdown profiles. Our results show that if the linear solution corresponding to a given set of parameter is unstable, then rupture can take place. Whether a ring- or line-like rupture emerges is a nonlinear phenomenon but line rupture replaces a ring rupture as the parameters vary so that the maximum linear growth rate increases. In situations in which thin electrical double layers form at the wall and interface, and linear theory predicts instability, we have discovered some intriguing non-uniform steady states that are also dynamically stable because they are computed using a time-marching numerical method.

In figure 6, we plot the minimum film height as a function of time for all parameter values shown in figure 5, with figure 5(*a*), (*b*) and (*c*) depicting the evolution to the final profiles shown in the first, second and third rows, respectively, of the figure. We see from figure 6(*a*), which varies $\hat{Q}$, that the time to touchdown decreases as $\hat{Q}$ increases. This is expected because an increase in $\hat{Q}$ corresponds to an increase in the electrostatic forces that act to attract the interface to the wall (equivalently, larger linear growth rates are found as $\hat{Q}$ increases). Figure 6(*b*), on the other hand, shows that for fixed values of $\hat{Q} = 1$, $\Phi = 2$, an increase in $\bar{\chi}$ leads to increased

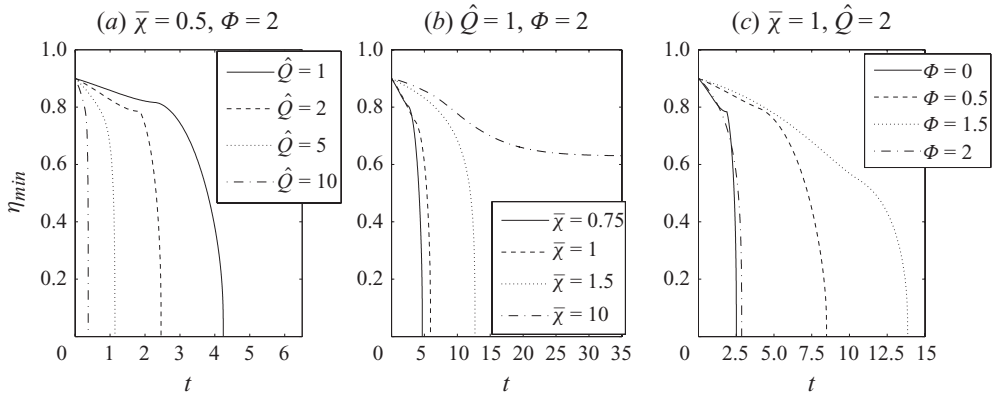

FIGURE 6. Minimum film height η_{min} as a function of time for the parameters of figure 5. The initial film height is $\eta = 1 - A\cos(\pi z/L)$, where $L = 2\pi$ and $A = 0.1$.

rupture times. This behaviour can be explained by noting that the instability-inducing attractive force due to the electrokinetics decreases as the Debye length relative to the film thickness decreases (quantitatively, maximal linear growth rates decrease with moderate values of $\bar{\chi}$; see the left instability island in figure 2*c* for example). For $\bar{\chi} = 10$, however, the minimal film thickness decreases initially in response to linear instability, but then asymptotes to a constant value as time increases, confirming the non-uniform steady state depicted in figure 5(*h*) discussed earlier. Figure 6(*c*) shows the film reaching the wall in the shortest time for $\Phi = 0$ and 2. These results can be explained by appealing to those presented in figure 2 obtained from the linear stability analysis: for $\bar{\chi} = 1$ and $\hat{Q} = 2$, the maximal linear growth rate is largest for $\Phi = 0$; this is followed by the maximal growth rate associated with $\Phi = 2$, $\Phi = 1/2$ and $\Phi = 1$.

The evolution of the film to the steady-state profile and the potential across the film at $z = 0$ (the location of the minimum height) are plotted in figure 7. On the basis of linear theory the initial perturbation, for $\bar{\chi} \gg 1$, is unstable to capillary forces near $\eta \sim 1$ and the electric field introduces a weak repulsive force. As time increases, the film moves closer to the wall, which brings the wall and interfacial Debye layers closer together and increases the repulsive electrokinetic force. At a sufficiently long time the film attains a stable steady-state profile at a height where the capillary and electrokinetic forces balance. Examining the evolution equation (2.67) in the limit $\bar{\chi}\eta \gg 1$, the electrokinetic term can be simplified, yielding

$$\eta_t + \left[\eta^3\eta_{zzz} + \eta^3\eta_z\left(1 - \frac{2\Phi\hat{Q}\bar{\chi}^3}{\exp(\bar{\chi}\eta)}\right)\right]_z = 0. \tag{3.4}$$

In this form it is clear that the electrokinetic part is always positive and introduces a repulsive force. Figure 7(*c*,*d*) depicts the dependence of the minimum steady-state film height on $\bar{\chi}$ with Φ varying parameterically, for two values of $\hat{Q}$. From (3.4) we can see that the repulsive electrokinetic force increases with Φ and $\hat{Q}$, causing the steady minimum film height to increase as shown in figure 7(*c*,*d*). On the other hand, increasing $\bar{\chi}$ thins the Debye layers, which decreases the repulsive force and the stable film height is closer to the wall. Below a critical value of $\bar{\chi}$, determined by linear stability theory as a function of Φ and $\hat{Q}$, the film is stable as indicated

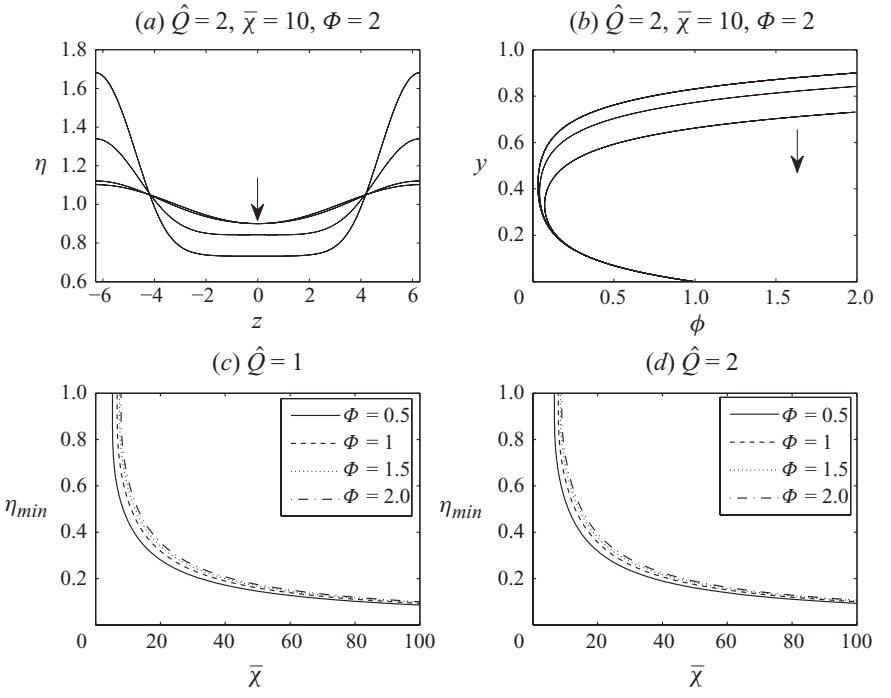

FIGURE 7. Evolution of the film to the steady-state profile (a) and potential across the film at $z=0$ (b) for $\hat{Q}=2$, $\bar{\chi}=10$ and $\Phi=2$ and the minimum film height as a function of the parameters $\hat{Q}$, $\bar{\chi}$ and Φ (c,d). The lines in (a,b) correspond to dimensionless times, $t=0.1$, 1, 10, 100, 1000, and the arrow shows the direction of increasing time.

by $\eta_{min}=1$. A further increase in the Debye length (below $\bar{\chi}=4.0$ shown in figure 7) brings the film into an unstable regime, discussed previously, with $\eta_{min}=0$. For larger values of $\bar{\chi}$, the location of the minimum film height moves closer to the wall but with a flattening of the profile in time. As a result, $\bar{\chi}\eta \gg 1$, even for small Debye lengths and finite time, touchdown of the film does not appear to be possible.

3.3. *Finite-time touchdown: scalings and self-similar solutions*

It is evident from the simulations that touchdown of the interface on the wall can occur in finite time. It is sufficient to study the touchdown dynamics using (3.1), which is valid for $\bar{\chi}\eta \ll 1$. The reason for this is that we are seeking a local description of touchdown solutions which by definition must satisfy $\eta \ll 1$, implying that the emerging structures will satisfy (3.1) asymptotically (the evolution and singular solutions of (3.1) have been considered by Wang 2009). The positive quantity $\hat{Q}(1-\Phi)^2$ can be scaled out of (3.1) by setting $\eta=(\hat{Q}(1-\Phi)^2)^{1/3}\hat{\eta}$ and $t=\hat{t}/(\hat{Q}(1-\Phi)^2)$. In the limit $\Phi\to 1$ (i.e. $\beta\to 0+$), the next-order term in the expansion of the electrokinetic contribution is weaker than the $\eta^3\eta_z$ term and the interface then follows a scaling of $t^{-1/2}$ as time progresses without rupture. The resulting scaling in this case is precisely that of the Hammond equation (Jones & Wilson 1978; Hammond 1983) as shown in figure 8(d).

We anticipate that the touchdown dynamics are self-similar. In order to extract the similarity scalings, we balance the electrokinetic and capillary pressures, and adopting a similarity scaling

$$\eta=\tau^{\alpha}\mathscr{H}(\zeta), \qquad \zeta=(z-z_{touchdown})/\tau^{\gamma}, \tag{3.5}$$

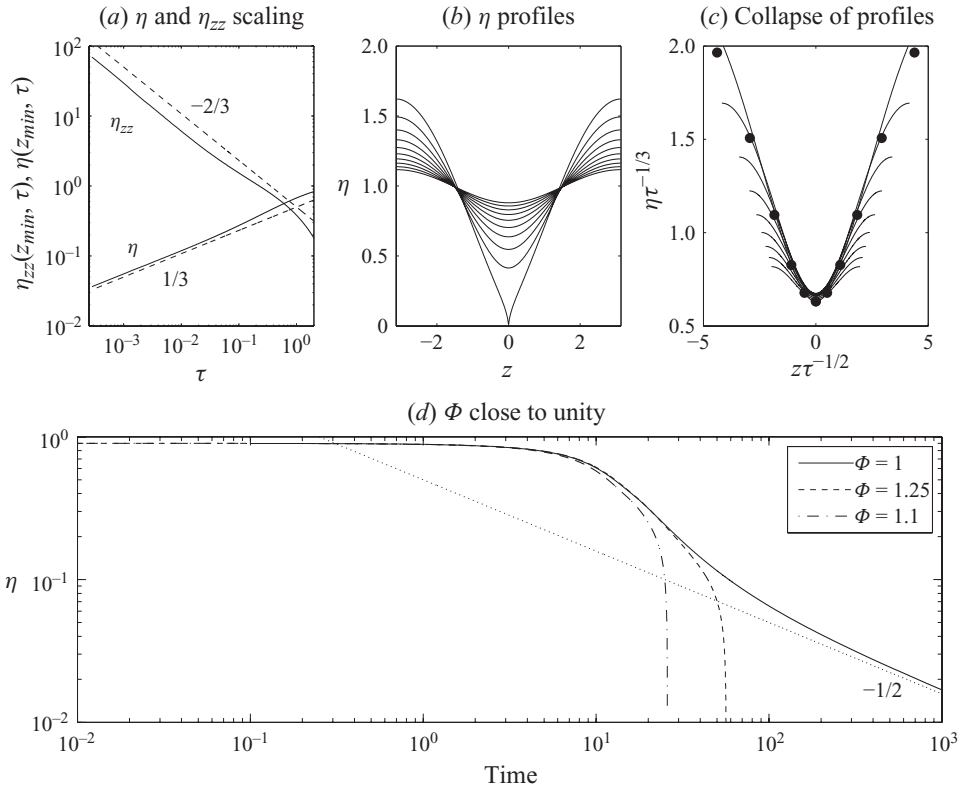

FIGURE 8. The behaviour of the solution near touchdown in the Debye–Hückel limit. The parameters in (*a–c*) are $\overline{\chi}=1$, $\hat{Q}=1$, $\Phi=2$ with initial condition $\eta=1-A\cos(\pi z/L)$ with $A=0.1$ and $-L<x<L$, $L=\pi/k$ and $t_{touchdown}=2.82615$. (*a*) The convergence to the similarity scalings as touchdown is approached. (*b*) The height profiles and (*c*) their collapse to a similarity ODE. In (*c*), the 10 profiles are from $Nt_{touchdown}/10$ for $N=1,2\ldots10$, and the dots are from the solution to the similarity ODE (3.6). (*d*) The evolution of η with time for $\Phi=1, 1.1, 1.25$ showing that for $\Phi=1$ the film thins as $t^{-1/2}$; this scaling is denoted by the dotted line.

where $\tau=(t_{touchdown}-t)$, gives $\alpha=1/3$ and $\gamma=1/2$. To confirm these scalings we present numerical solutions that follow the evolution to rupture for a typical case having $\hat{Q}=1$, $\Phi=2$ and $\overline{\chi}=1$; the results are depicted in figure 8. Figure 8(*a*) shows the evolution of the minimum value of η and the corresponding curvature η_{zz}. According to the order-of-magnitude arguments, the behaviour is expected to be $\eta(z_{min},\tau)\sim\tau^{1/3}$ and $\eta_{zz}(z_{min},\tau)\sim\tau^{-2/3}$ as $\tau\to0$, and these predictions are fully confirmed by the log–log plots in figure 8(*a*). Figure 8(*b*) shows the evolution of the interface to touchdown and includes the final computed profile characterized by $\eta_{min}<10^{-5}$. These self-similar scalings also indicate that $\eta_z(z_{min},\tau)\sim\tau^{-1/6}$, implying that the slope becomes large as rupture is approached, which ultimately renders the present long-wave theory invalid. In a related study of the planar film rupture in the presence of van der Waals forces, Zhang & Lister (1999) also predict a cusp singularity. In both cases, as the singularity is approached the disparity of scales is no longer valid and the full Stokes and electrokinetic equations need to be considered in the vicinity of the touchdown singularity, with the solution found here setting the far-field conditions for the associated elliptic problems. We note that the direct simulations of Wang (2009)

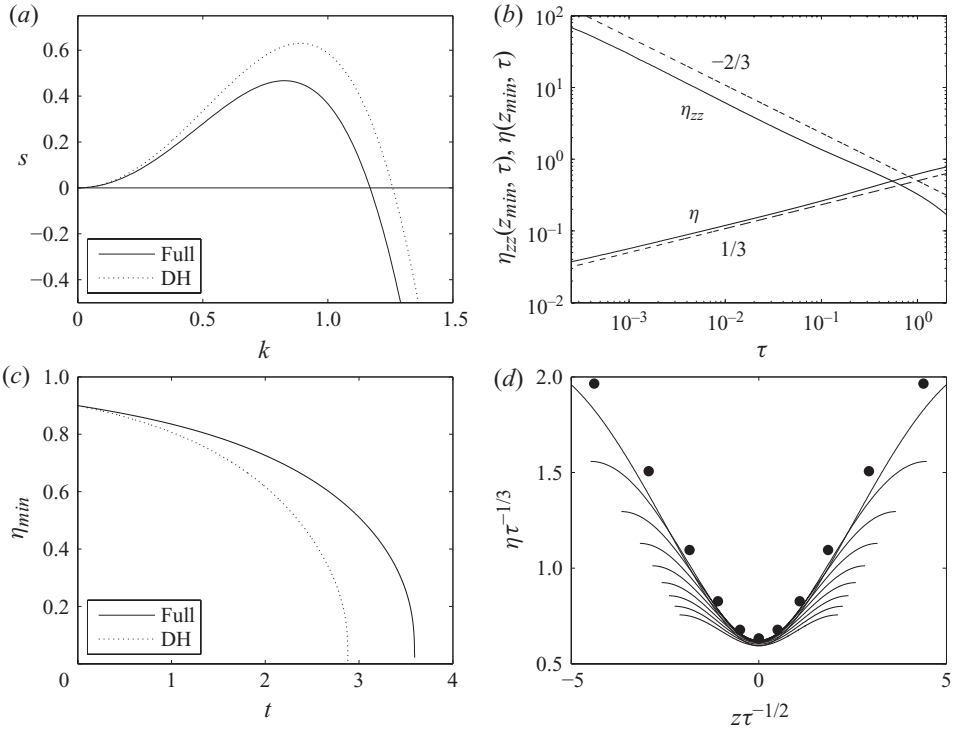

FIGURE 9. The behaviour of the solution near touchdown for the full Poisson–Boltzmann model. The parameters are $\overline{\chi} = 1$, $\hat{Q} = 1$, $\Phi = 2$ with initial condition $\eta = 1 - A\cos kx$ with $k = k_{max}$, $A = 0.1$ and $-L < x < L$, $L = \pi/k$. (*a*) The dispersion curves for the full versus Debye–Hückel cases, k_{max} is the value of k for which the growth rate is largest. (*b*) The scalings for the minimal value of η and the maximal value of η_{zz}. (*c*) The evolution of the minimal value of η versus time for the full and DH models. (*d*) The collapse of the height profiles under the scalings to the similarity solution (dotted).

predict touchdown singularities in good qualitative agreement with what is found here; the details very close to the singularity, however, are different as expected.

The asymptotic self-similar behaviour of the interface is described by the scaling function $\mathscr{H}(\zeta)$; substituting the scalings (3.5) into either of (3.1), (2.66) or (2.67) and retaining the dominant terms for $\tau \ll 1$ yields the ordinary differential equation (ODE)

$$-\tfrac{1}{3}\mathscr{H} + \tfrac{1}{2}\zeta\mathscr{H}' + [\mathscr{H}^3\mathscr{H}''' + \hat{Q}(1-\Phi)^2\mathscr{H}']' = 0, \tag{3.6}$$

which must be solved for $-\infty < \zeta < \infty$. The asymptotic behaviour of solutions for large ζ is $\mathscr{H} \sim A\zeta^{2/3}$, and values of $A, H(0), H''(0)$ consistent with that behaviour were found numerically. The resulting numerical solution of (3.6) is represented by heavy dots in figure 8(*c*). Using the evolving profiles from figure 8(*b*) and the ansatz (3.5), we obtain a sequence of scaling functions that converge to the solution of (3.6), as confirmed by the results in figure 8(*c*); as expected, agreement improves as the singular time is approached. The parameters in this figure are for a regime where the film is linearly unstable and $\overline{\chi}\eta$ becomes sufficiently small that (3.1) holds.

For completeness we consider analogous numerical solutions for the full Poisson–Boltzmann system governed by (2.66) coupled with (2.51), rather than using the Debye–Hückel version (2.67). Results from numerical simulations are given in figure 9(*a*)–(*d*) for parameter values $\bar{\chi} = 1$, $\hat{Q} = 1$ and $\Phi = 2$. Figure 9(*a*) depicts

the linear dispersion relation and shows that the growth rates of the full system are overestimated by those of the Debye-Hückel approximation. As a result, the time to touchdown for the present simulations is larger for the Poisson–Boltzmann system as confirmed by the results in figure 9(*c*). As rupture takes place and the value of $\bar{\chi}\eta$ becomes small locally, the same self-similar structures described above are expected to govern the dynamics – this is because the Poisson–Boltzmann equation (2.51) linearizes for $\bar{\chi}\eta \ll 1$ and leads to the Debye–Hückel version (2.67). These predictions are confirmed by the numerical solutions; figure 9(*b*) shows the evolution, as the rupture time is approached, of η and η_{zz} at the minimum interface location point $z = z_{min}$. The logarithmic plot predicts the behaviour $\eta(z_{min}, t) \sim \tau^{1/3}$ and $\eta_{zz}(z_{min}, t) \sim \tau^{-2/3}$, in complete agreement with the self-similar theory outlined above. Figure 9(*d*) compares the profiles near touchdown with the self-similar solution of (3.6) (the latter depicted by heavy dots); as time tends closer to the rupture time $\tau = 0$, the computed profiles converge to the self-similar scaling function $\mathscr{H}$ with excellent agreement between the two.

4. Conclusions

This paper explores the influence of electrokinetics on the dynamics of an annular electrolyte film that surrounds a perfectly conducting fluid core in a horizontal cylinder. A novel evolution equation for the interfacial position has been derived in the thin-film limit which includes the competing effects of capillary and electrokinetic forces. The latter are calculated by solving a scaled Poisson–Boltzmann equation in the film or its Debye–Hückel approximation. There are three parameters in the problem: a scaled electric Weber number $\hat{Q}$ representing the ratio of electrostatic to capillary forces, a scaled dimensionless inverse Debye length $\overline{\chi}$, and Φ denoting the ratio of interfacial to wall potentials. The asymptotic analysis is carried out in the lubrication limit, and canonical scalings are introduced in order to allow capillary and electrokinetic effects to compete. Linear aspects of the flow are analysed and extensive numerical simulations into the nonlinear regime have been carried out. The computations predict three canonical evolution regimes depending on the controlling parameters.

When disturbances to the interface are linearly stable, the flow is damped and produces a uniform perfectly cylindrical interface – this typically happens when the Debye length is comparable to the undisturbed film thickness, that is $\overline{\chi} = O(1)$. A typical case can be seen in figure 2(*c*) for $\hat{Q} = 1$, $\Phi = 1/2$ and $\overline{\chi} = 3$, which predicts damping, and the corresponding voltage potential in the film shown in figure 4(*b*), where it is concluded that the electric field acts to repel the interface from the wall.

If the parameters are such that there exist linearly unstable modes then the ultimate evolution is either a rupture of the annulus in finite time or the development of stable steady states characterized by spatially non-uniform interfacial shapes. These phenomena are only possible if electrokinetic effects are present and cannot occur in the system studied by Hammond (1983) and Lister *et al.* (2006). In addition, the shapes of ultimate ruptured states can be controlled by varying the governing parameters to produce what we have termed as ring rupture (arising when touchdown takes place simultaneously at two points on the wall; see figure 5*a* for example) or line rupture characterized by a single touchdown point as in figure 5(*c*), for example. Our computations show that ring rupture can be converted to line rupture in three different ways: First, by increasing the electric Weber number $\hat{Q}$ (all other parameters being equal) and thus imposing a larger attractive force between the interface and the

wall (see figure 5*a–d*); second, by increasing $\overline{\chi}$ to moderate values so that the scaled Debye length is initially large but then decreases and induces a larger attraction between the interface and the wall (see figure 5*e–h*, excluding the results of figure 5*h*, whose emergence is discussed below); third, by increasing Φ so that the interfacial potential increases relative to that of the wall and again inducing a larger electrostatic attraction between the interface and the wall (see figure 5*i–l*). In all cases in which rupture occurs, our analytical and computational results predict that the structures are self-similar, with the minimum film thickness scaling as $(t_{touchdown} - t)^{1/3}$, where $t_{touchdown}$ denotes the touchdown time.

The third canonical evolution regime is a novel nonlinear phenomenon discovered here for the electrokinetic systems under investigation. Extensive computations show that it is possible to attain a balance between capillary and electrokinetic forces to produce spatially non-uniform steady states. Linear theory cannot predict these but a band of linearly unstable modes must be present in order to produce a non-uniform state. The computed steady states are stable in the sense that they are calculated by solving initial value problems, and we have established that they emerge when the value of $\overline{\chi}$ is moderately large; see for example figures 5(*h*) and 7. In this regime, the scaled Debye length is small relative to the undisturbed film thickness and electrical double layers form at the interface and the wall. These layers act to reduce the impact of capillary instability by their mutual repulsion, and in linear terms the maximum growth rate of the instability is reduced; see for example the lower growth rates that are obtained at large $\overline{\chi}$ in figure 2(*c,d*). Nonlinearly, however, the system evolves to the non-uniform steady states shown here. The collective results of figure 7 show that if the steady states are stable (in the sense that they are obtained by solving an initial value problem) then the minimum film thickness decreases as $\overline{\chi}$ increases; see figure 7(*b,c*). Physically, this is understood by noting the increase in the linear growth rates as $\overline{\chi}$ increases and the thickness of the electrical double layers decreases, thus thwarting their mutual repulsion.

D. T. P. was supported in part by the National Science Foundation grant DMS-0707339. O. K. M. and R. V. C. acknowledge support from the EPSRC through the platform grant EP/E046029/1. R. V. C. also acknowledges support from NSERC through their Discovery Grant scheme.

REFERENCES

Aul, R. W. & Olbricht, W. L. 1990 Stability of a thin annular film pressure-driven, low-Reynolds number flow through a capillary. *J. Fluid Mech.* **215**, 585–599.

Campana, D., Di Paolo, J. & Saita, F. 2004 A two-dimensional model of Rayleigh instability in capillary tubes: surfactant effects. *Intl J. Multiphase Flow* **30**, 431–454.

Chandrasekhar, S. 1961 *Hydrodynamic and Hydromagnetic Stability*. Oxford University Press.

Chang, H.-C. & Demekhin, E. A. 1999 Mechanism for drop formation on a coated vertical fibre. *J. Fluid Mech.* **380**, 233–255.

Chang, H.-C. & Yeo, L. Y. 2010 *Electrokinetically Driven Microfluidics and Nanofluidics*. Cambridge University Press.

Chang, H.-C. & Yossifon, G. 2009 Understanding electrokinetics at the nanoscale: a perspective. *Biomicrofluidics* **3**, 012001.

Craster, R. V. & Matar, O. K. 2006 On viscous beads flowing down a vertical fibre. *J. Fluid Mech.* **553**, 85–106.

Craster, R. V. & Matar, O. K. 2009 Dynamics and stability of thin liquid films. *Rev. Mod. Phys.* **81**, 1131–1198.

Everett, D. H. & Haynes, J. M. 1972 Model studies of capillary condensation. 1. Cylindrical pore model with zero contact angle. *J. Colloid Interface Sci.* **38**, 125–137.

Frenke, A. L., Babchin, A. J., Levich, B. G., Shlang, T. & Sivashinsky, G. I. 1987 Annular flow can keep unstable flow from breakup: nonlinear saturation of capillary instability. *J. Colloid Interface Sci.* **115**, 225–233.

Gauglitz, P. A. & Radke, C. J. 1988 An extended evolution equation for liquid-film break up in cylindrical capillaries. *Chem. Engng Sci.* **43**, 1457–1465.

Georgiou, E., Papageorgiou, D. T., Maldarelli, C. & Rumschitzki, D. S. 1991 The double layer-capillary stability of an annular electrolyte film surrounding a dielectric-fluid core in a tube. *J. Fluid Mech.* **226**, 149–174.

Gitlin, I., Stroock, A. D., Whitesides, G. M. & Ajdari, A. 2003 Pumping based on transverse electrokinetic effects. *Appl. Phys. Lett.* **83**, 1486–1488.

Glasner, K. B. & Witelski, T. P. 2003 Coarsening dynamics of dewetting films. *Phys. Rev.* E **67**, 016302.

Goren, S. L. 1962 The instability of an annular thread of fluid. *J. Fluid Mech.* **12**, 309–319.

Grotberg, J. B. & Jensen, O. E. 2004 Biofluid mechanics in flexible tubes. *Annu. Rev. Fluid Mech.* **36**, 121–147.

Hagerdon, J. G., Martyn, N. S. & Douglas, J. F. 2004 Breakup of a fluid thread in a confined geometry: droplet–plug transition, perturbation sensitivity, and kinetic stabilization with confinement. *Phys. Rev.* E **69**, 056312.

Halpern, D. & Grotberg, J. B. 2003 Nonlinear saturation of the Rayleigh instability due to oscillatory flow in a liquid-lined tube. *J. Fluid Mech.* **492**, 251–270.

Hammond, P. S. 1983 Nonlinear adjustment of a thin annular film of viscous fluid surrounding a thread of another within a circular cylindrical pipe. *J. Fluid Mech.* **137**, 363–384.

Hosoi, A. E. & Mahadevan, L. 1999 Axial instability of a free-surface front in a partially filled horizontal rotating cylinder. *Phys. Fluids* **11**, 97–106.

Jensen, O. E. 1997 The thin liquid lining of a weakly curved cylindrical tube. *J. Fluid Mech.* **331**, 373–403.

Johnson, M., Kamm, R. D., Ho, L. W., Shapiro, A. & Pedley, T. J. 1991 The nonlinear growth of surface-tension-driven instabilities of a thin annular film. *J. Fluid Mech.* **233**, 141–156.

Jones, A. F. & Wilson, S. D. R. 1978 The film drainage problem in droplet coalescence. *J. Fluid Mech.* **87**, 263–288.

Joseph, D. D., Bai, R., Chen, K. P. & Renardy, Y. Y. 1997 Core-annular flows. *Annu. Rev. Fluid Mech.* **29**, 65–90.

Kalliadasis, S. & Chang, H.-C. 1994 Drop formation during the coating of vertical fibres. *J. Fluid Mech.* **261**, 135–168.

Kas-Danouche, S., Papageorgiou, D. T. & Siegel, M. 2009 Nonlinear dynamics of core-annular flows in the presence of surfactant. *J. Fluid Mech.* **626**, 415–448.

Keast, P. & Muir, K. H. 1991 Algorithm 688 EPDCOL: a more efficient PDECOL code. *ACM Trans. Math. Software* **17**, 153–166.

Kerchman, V. 1995 Strongly nonlinear interfacial dynamics in core-annular flows. *J. Fluid Mech.* **290**, 131–166.

Kliakhandler, I. L., Davis, S. H. & Bankoff, S. G. 2001 Viscous beads on vertical fibre. *J. Fluid Mech.* **429**, 381–390.

Lister, J. R., Rallison, J. M., King, A. A., Cummings, L. J. & Jensen, O. E. 2006 Capillary drainage of an annular film: the dynamics of collars and lobes. *J. Fluid Mech.* **552**, 311–343.

Maitland, G. C. 2000 Oil and gas production. *Curr. Opinion Colloid Interface Sci.* **5**, 301–311.

Moffatt, H. K. 1977 Behaviour of a viscous film on the outer surface of a rotating cylinder. *J. Mec.* **16**, 651–673.

Newhouse, L. A. & Pozrikidis, C. 1992 The Rayleigh–Taylor instability of a viscous-liquid layer resting on a plane wall. *J. Fluid Mech.* **217**, 615–638.

Olbricht, W. L. 1996 Pore-scale prototypes of multiphase flow in porous media. *Annu. Rev. Fluid Mech.* **28**, 187–213.

Oron, A., Davis, S. H. & Bankoff, S. G. 1997 Long-scale evolution of thin liquid films. *Rev. Mod. Phys.* **69**, 931–980.

Papageorgiou, D. T., Maldarelli, C. & Rumschitzki, D. S. 1990 Nonlinear interfacial stability of core-annular film flow. *Phys. Fluids* A **2**, 340–352.

Quéré, D. 1990 Thin-films flowing on vertical fibers. *Europhys. Lett*. **13**, 721–726.

Quéré, D. 1999 Fluid coating on a fiber. *Annu. Rev. Fluid Mech.* **31**, 347–384.

Ruyer-Quil, C., Treveleyan, P., Giorgiutti-Dauphiné, F., Duprat, C. & Kalliadasis, S. 2008 Modelling film flows down a fibre. *J. Fluid Mech.* **603**, 431–462.

Saville, D. A. 1997 Electrohydrodynamics: the Taylor–Melcher leaky-dielectric model. *Annu. Rev. Fluid Mech.* **29**, 27–64.

Squires, T. M. & Bazant, M. Z. 2004 Induced-charge electro-osmosis. *J. Fluid Mech.* **509**, 217–252.

Squires, T. M. & Quake, S. R. 2005 Micro-fluidics: fluid physics at the nanoliter scale. *Rev. Mod. Phys.* **77**, 977–1024.

Thorodsen, S. T. & Mahadevan, L. 1997 Experimental study of coating flows in a partially-filled horizontally rotating cylinder. *Exp. Fluids* **23**, 1–13.

Tsvelodub, O. Y. & Trifonov, Y. Y. 1992 Nonlinear waves on the surface of a falling liquid film. Part 2. Bifurcations of the first-family waves and other types of nonlinear waves. *J. Fluid Mech.* **244**, 149–169.

Vaynblat, D., Lister, J. R. & Witelski, T. P. 2001 Rupture of thin viscous films by van der Waals forces: evolution and self-similarity. *Phys. Fluids* A **13**, 1130–1140.

Wang, Q. 2009 Nonlinear evolution of annular layers and liquid threads in electric fields. PhD thesis, New Jersey Institute of Technology, Newark, New Jersey.

Wei, H.-H. & Rumschitzki, D. 2002 The linear stability of a core-annular flow in an asymptotically corrugated tube. *J. Fluid Mech.* **466**, 113–147.

Weidner, D. E., Schwartz, L. W. & Eres, M. H. 1997 Simulation of coating layer evolution and drop formation on horizontal cylinders. *J. Colloid Interface Sci.* **187**, 243–258.

Zhang, W. W. & Lister, J. R. 1999 Similarity solutions for van der Waals rupture of a thin film on a solid substrate. *Phys. Fluids* **11**, 2454–2462.